RESEARCH ARTICLE

Editor's Choice

**ADVANCED
MATERIALS
INTERFACES**
Open Access

www.advmatinterfaces.de

Mineral Interface Doping: Hydroxyapatite Deposited on Silicon to Trigger the Electronic Properties

Peter Thissen* and Roberto C. Longo

Doping silicon wafers without using highly toxic or corrosive chemical substances has become a critical issue for semiconductor device manufacturing. In this work, ultra-thin films of hydroxyapatite ($Ca_5(PO_4)_3OH$) are prepared by tethering by aggregation and growth (T-BAG), and further processed by spike annealing. Via in situ infrared (IR), the decomposition of hydroxyapatite and intermixing with the native silicon oxide is observed already at temperatures as low as 200 °C. Phosphate transport through the native silicon oxide is driven by a phase transformation into a more stable thermal oxide. At 700 °C, diffusion of phosphorus into the sub-surface region of oxide-free silicon is observed. In situ IR combined with electrical impedance spectroscopy (EIS), time-of-flight secondary ion mass spectrometry (ToF-SIMS), and X-ray photoelectron spectroscopy (XPS) measurements allows to conclude that the phosphorus is: i) transported through the silicon oxide barrier, ii)) diffused inside the oxide-free silicon, and iii) finally modified the electrical activity of the silicon wafer. To further explain the experimental findings, density-functional theory (DFT) is used to demonstrate the extent of the effect of phosphorus doping on the electronic nature of silicon surfaces, showing that even small amounts of doping can have a measurable effect on the electrical performance of semiconductor wafers.

1. Introduction

The increased demand for electronic devices observed in recent years requires sophisticated technologies that are not always eco-friendly. Within this context, monolayer doping (MLD) has become a substantial improvement toward the electrical activation of silicon substrates.[1–5] Conventional doping methods such as spin-on glass doping,[6] ion implantation,[7,8] or plasma doping[9] have yielded promising results,[3] although challenges still remain, especially in regards to nonhomogeneous dopant distributions.[10–12] MLD comprises: i) the functionalization of a semiconductor surface with n- or p-dopant-containing molecule, and ii) the thermal diffusion of the dopant into the surface,[3,4] where self-assembled monolayers (SAMs) yield consistent dopant coverage. To avoid SAM desorption, a capping layer such as SiO_2 or Al_2O_3 was typically used.[3]

MLD utilizes the crystalline nature of semiconductor materials and the self-limiting nature of surface reactions to form highly uniform, self-assembled, and covalently bonded dopant-containing monolayers, followed by a subsequent annealing step for the interdiffusion of dopants.[3] The monolayer formation reaction is self-limiting, thereby resulting in a deterministic coverage of dopant atoms on the surface. MLD differs from other conventional doping techniques such as spin-on-dopants (SODs) and gas phase doping in the accurate dopant dose control. Such control in MLD is attainable due to the self-limiting formation of covalently attached dopants on the surface, while SODs just rely on the thickness control of the spin-on oxide, and the gas phase doping technique depends on the control of dopant gas flow rate. Therefore, the dose control in MLD can yield exact tuning of the resulting dopant profile.

As opposed to ion implantation, MLD does not involve the energetic introduction of dopant species into the semiconductor matrix, which can easily lead to crystal damage. Defects such as interstitials and vacancies are inevitably generated during ion implantation, which can further interact with the dopants to broaden the junction profile. This effect is known as transient-enhanced diffusion (TED) and severely limits the formation of good-quality ultra-shallow junctions (USJ). Also, stochastic variation in the dopant positioning and severe stoichiometric imbalance can be induced in binary and tertiary semiconductor compounds by using implantation techniques. In contrast, all MLD dopant atoms are thermally diffused from the crystal surface to the bulk, therefore the dopant profile can be easily controlled by the thermal budget. MLD can be classified as a limited source model, something highly desirable for controlled USJ fabrication with high uniformity and low stochastic variation. Combining both the dopant dose uniformity and coverage control, MLD is

P. Thissen
Karlsruher Institut für Technologie (KIT)
Institute of Concrete Structures and Building Materials
76131 Karlsruhe, Germany
E-mail: peter.thissen@kit.edu
R. C. Longo
Tokyo Electron America, Inc.
Austin, Texas 78741, United States

especially attractive for doping nonplanar devices such as gate-all-around field effect transistors (GAA-FETs) or even nanowires. For instance, high-quality sub-5 nm USJ has been demonstrated in silicon using MLD techniques.[4] Furthermore, compared to low-energy ion implantation into a screening film followed by in-diffusion,[13,14] MLD requires a lower thermal budget, thus allowing conformal doping on topographic features.

The MLD process is applicable for both n- and p-doping of various nanostructured materials, including conventional planar substrates, nanobelts, and nanowires, which are fabricated by either the 'bottom-up' or 'top-down' approaches, therefore making it a highly versatile technique for various applications. Typically, in p-type doping of silicon, a covalently anchored monolayer of allylboronic acid pinacol ester is formed on the surface as the boron precursor, while a monolayer of diethyl 1-propylphosphonate is often used as the phosphorus precursor in n-type doping.[3] For example, during the formation of USJ, combining phosphorus-MLD and conventional spike annealing, a record 5 nm junction (down to 2 nm–the resolution limit of secondary-ion mass spectrometry) with noncontact resistivity measurements of $\approx$5000 Ω cm^{-1} was reported, consistent with the predicted values from the dopant profile.[4] Notably, $\approx$70% of the dopants are electrically active as the MLD process utilizes an equilibrium-based diffusion mechanism.[4]

From a practical perspective, the MLD process comprises several steps: i) preparation of an oxide-free semiconductor surface, ii) functionalization of the surface with a molecule containing the desired n- or p-dopant, and iii) thermal diffusion of the dopant into the near-surface region ($\approx$nm). The self-limiting nature of SAMs of MLD provides uniform coverage of a well-defined quantity of dopant atoms. A subsequent high-temperature annealing step drives the dopant atoms into the semiconductor via diffusion. To avoid the desorption of the SAM, an oxide capping layer (e.g., SiO$_2$ or Al$_2$O$_3$) is typically deposited on top of the SAM, which has the undesirable side effect of trapping carbon impurities from the organic molecular precursor, eventually leading to the deactivation of the electrical activity of the dopants. Alternatively, the silica-like architecture or some molecular precursors allow the in situ generation of a SiO$_2$ capping nanolayer before annealing.

In this paper, we make use of in situ infrared spectroscopy (IR) to investigate a fundamentally different grafting method, based on a recent finding that allows direct attachment of dopants on a silicon wafer. The process is called tethering by aggregation and growth (T-BAG), which was initially developed for the deposition of SAMs of phosphonic acids.[15] Recent investigations showed that the preparation technique is reproducible for the use of lamellar structured minerals.[16] Here, the preparation was adapted for the deposition of thin films of phosphate mineral particles, more specifically hydroxyapatite (Ca$_5$(PO$_4$)$_3$(OH)). In order to unravel the effects of doping at the atomic scale, using density-functional theory (DFT) we developed phosphorus-doped silicon surface models with different dopant distributions and concentrations, to study specific, measurable properties such as the electronic work function. Our simulations corroborate that even for low, near-surface doping concentrations, mineral interface doping (MID) provides a quantifiable improvement of the electrical activation across the entire doping profile.

2. Methodology

2.1. Sample Preparation

P-type (boron-doped, resistivity of 24–34 Ω cm) float-zone (FZ) Si(111) wafers, polished on both sides, were cut into 1 cm $\times$ 3 cm pieces (thickness = 500 μm) for infrared transmission measurements. Oxides were chemically cleaned by 30 min of exposure to an 80 °C solution of 3:1 concentrated (18 M) H$_2$SO$_4$/30% H$_2$O$_2$(aq) (hereafter referred to as piranha solution) to remove organic contamination. The wafer was rinsed with deionized water and dried in a stream of N$_2$. Subsequently, the silicon wafer was immersed in a dispersion of hydroxyapatite (HAp, Ca$_5$(PO$_4$)$_3$(OH)) from Omikron GmbH, both with 99% pureness, respectively, and with a concentration of 1 mg mL^{-1}. The dispersion was heated at 60 °C until complete evaporation ($\approx$6 h) of the liquid and the mineral particles covered both sides of the wafer surface.[15–17]

The coated wafer was mounted on a heatable sample holder made of tantalum, under N$_2$ purging in an oxygen-free atmosphere, and analyzed with IR transmission spectroscopy. The temperature of the sample was increased stepwise from room temperature to 900 °C, whereas the spectra were recorded at room temperature (RT), (**Figure 1**).

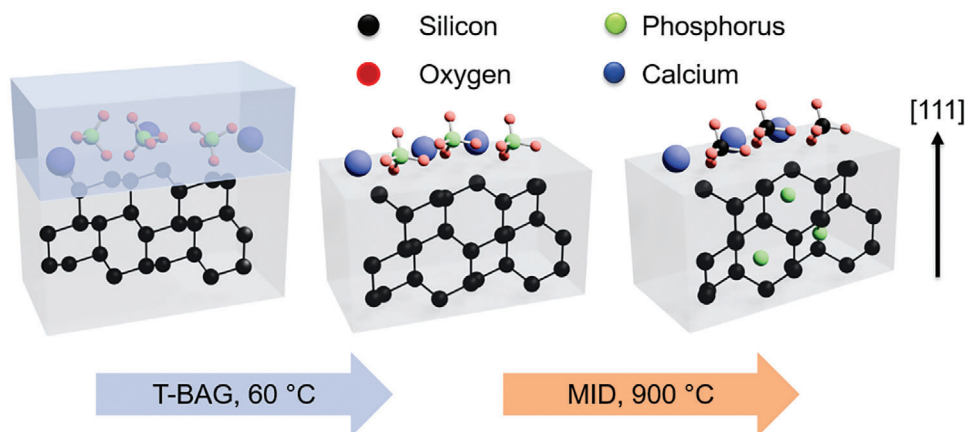### 2.2. Fourier Transform Infrared Spectroscopy (FT-IR)

The FT-IR spectra were recorded on a Bruker Vertex V70 spectrometer equipped with a deuterated-triglycine sulfate (DTGS) detector. 1024 scans in the 7500–400 cm^{-1} spectral range were recorded with a resolution of 4 cm^{-1}.

2.3. Electrochemical Impedance Spectroscopy (EIS)

Impedance spectroscopy of the coated wafer before and after heating was performed using an IMPEDANCE ANALYZER IM3570 (HIOKI) R, L, C measuring device operated at room temperature in the frequency range of 8 Hz–8 MHz, using tantalum clamping contacts with a diameter of 1 mm.

2.4. X-ray Photoelectron Spectroscopy (XPS)

XPS analysis was performed with a Quantum 2000 Scanning ESCA Microprobe (Physical Electronics, USA) spectrometer, equipped with a concentric hemispherical analyzer under ultra-high vacuum (UHV) conditions (10^{-9} mbar) using an Al Kα1,2-radiation source. Spectra were recorded at 45° take-off angle with respect to the surface. A sample area of 100 μm $\times$ 100 μm was analyzed with a pass energy of 46.95 eV for survey and 11.75 eV for detailed elemental scans. To compensate for charging, a flood gun with an electron energy of 2 eV was used. Deconvolution of peaks was done using CASA XPS software, whereas peaks were fitted using Shirley background, Gaussian/Lorentzian (GL) line shapes, and a Marquardt–Levenberg optimization algorithm.

**ADVANCED
SCIENCE NEWS**

www.advancedsciencenews.com

**ADVANCED
MATERIALS
INTERFACES**

www.advmatinterfaces.de

Figure 1. Schematic description of 1) tethering by aggregation and growth @ 60 °C and 2) mineral interface doping @ 900 °C.

2.5. Time-of-Flight Secondary-Ion-Mass-Spectrometry (ToF-SIMS)

The ToF-SIMS analysis was carried out on a gridless reflectron-based ToF-SIMS V (ION-TOF GmbH, Muenster, Germany), equipped with a bismuth-cluster ion source. All spectra and images were obtained using Bi^{1+} primary ions at 25 keV energy in the high current bunched mode, with a mass resolution of $m/\Delta m \geq 6000$ @ ^{30}Si. The beam diameter was ≈ 3–5 µm. The Bi primary beam was rastered on a 100×100 µm^2 field of view, and 128×128 pixels were recorded. Depth profiling was performed in full interlaced mode with a 40 nA and 0.5 keV energy Cs^+ beam, rastered across 300×300 µm^2. The measured data was transformed into quantitative values with the help of the NIST Standard Reference Material, 2133, Phosphorus Implant in silicon depth profile standard.

3. Computational Methods

Calculations were performed using DFT within the generalized gradient approximation, as implemented in the VASP simulation package.[18,19] The projector-augmented wave scheme (PAW) was used to describe the electron-ion interaction,[20] whereas the electronic wave functions were expanded into plane waves with kinetic energy up to 500 eV. The PBE functional was used to describe the electron exchange and correlation interactions within the GGA.[21] The Si(111) surface was modeled by periodically repeated slabs of 8 atomic layers, with a vacuum region equivalent to 16 atomic layers. The surface was passivated at the bottom by hydrogen atoms, and all the layers except the bottom one, as well as adsorbed phosphorus atoms, were allowed to relax until a tolerance of 10^{-5} eV and 10 meV Å^{-1} in the energies and forces, respectively. Brillouin zone integration was performed using a $4 \times 4 \times 1$ k-mesh within the Monkhorst–Pack scheme.[22]

To correlate the computational results with the experimental doping process using thin films of phosphate mineral particles, we obtained the work function of the Si(111) surface for different phosphorus concentrations and configurations. The work function provides a measurement of the ease with which electrons can be extracted from the system, that is, to transport electrons from the Fermi level to the vacuum, and it is typically obtained using the local potential (including exchange and correlation energies):[23]

$$\varphi = E_v - E_F \tag{1}$$

where E_v and E_F are the vacuum level and Fermi energy, respectively. The lower the work function, the easier to free an electron from the solid, which is an undesirable effect. Therefore, doping levels introduced at the surface of the semiconductor can have a drastic effect on the electrical performance. Phosphorus adsorption energies (E_{ads}) were obtained with the formula:

$$E_{ads} = E_{tot} - E_{Si} - n \times \mu(P) \tag{2}$$
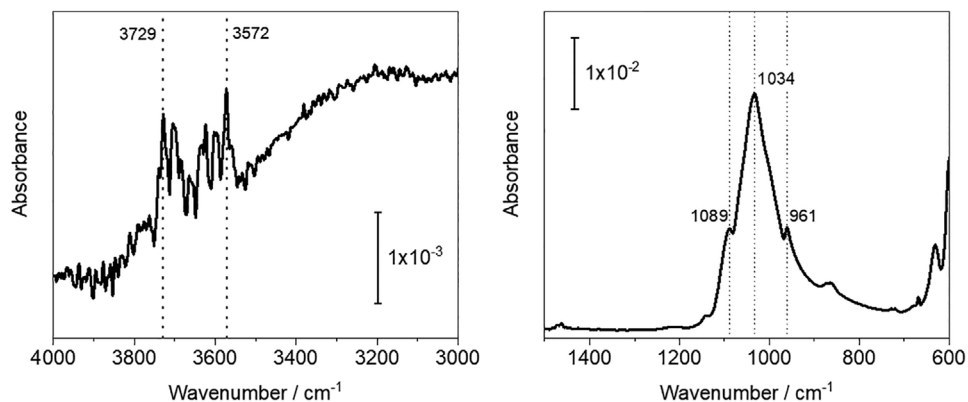
where E_{tot} is the total energy of the system, E_{Si} is the energy of the Si(111) surface, and $\mu(P)$ is the chemical potential of Phosphorus. In this work, we used the red phosphorus as the reference state. Although P_4 tetrahedral white phosphorus is regarded as the ground-state allotrope,[24] amorphous monoclinic red phosphorus provides a more suitable reference for adsorption energy calculations involving only a few phosphorus atoms.

4. Results and Discussion

4.1. Experimental Doping of Si Wafers

Silicon samples were first cleaned, in order to take a reference IR measurement. Subsequently, the T-BAG process was carried out and a second IR spectra was obtained, depicted in **Figure 2**, with the first measurement used as a reference. Adsorption of hydroxyapatite on the silicon wafer can be neatly observed. Three peaks appear at 1089, 1034, and 961 cm^{-1}, characterized as asymmetric stretching vibrations of phosphate groups.[25]

The next step of our experiment consists of a stepwise increase of the temperature by 800 °C, keeping the temperature at each step for 10 s, and then allowing the system to cool down again to the initial temperature. **Figure 3** shows the corresponding IR spectra as a function of the temperature. The spectra are always referred to the previous temperature, in order to differentiate the features corresponding to each separate heat step.

**ADVANCED
SCIENCE NEWS**

www.advancedsciencenews.com

**ADVANCED
MATERIALS
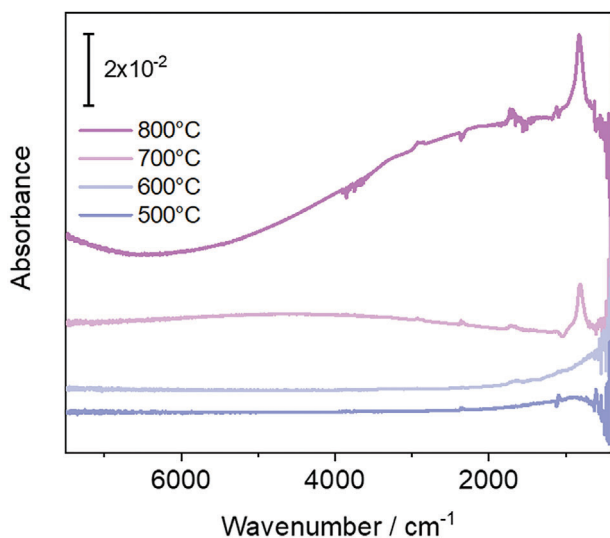INTERFACES**
Open Access

www.advmatinterfaces.de

Figure 2. FT-IR spectra of hydroxyapatite on Si(111). Measurements are referred to as the cleaned wafer.

Figure 3 shows a broad negative band between 3670 and 2570 cm^{-1} at 100 °C, while the release of gaseous CO_2 is observed at 2364 and 2336 cm^{-1} (Figure 3C). At 200 °C, a negative band at 2345 cm^{-1} and a broad band between 3700 and 2550 cm^{-1} are observed (Figure 3C). Both bands correspond to O—H stretching vibrations. The correlated bending vibration of water is observed at 1670 cm^{-1} (not shown). At 300 °C, a new shift of the P—O stretching vibrations at 1145 and 1084 cm^{-1} to lower wavenumbers is observed (Figure 3D), after the loss of the structural water and the surface reactions. The decarbonisation is accompanied by a loss of ν(CaO—H) at 3572 cm^{-1}, indicating a

surface reorganization of the HAp structure. Then, at 700 °C, the sample is water-free. Followed by the release of CO_2 and H_2O, the phosphate is transported through the native, chemical SiO_2, which is then transformed into thermal SiO_2. Thermal SiO_2 has lower absorptivity than chemical SiO_2, due to its more compact and crystalline structure. After heating the sample to 700 °C, a new IR signal appears in the range between 900 and 700 cm^{-1}, as a result of the chemical transformation of phosphate in contact with silicon. Finally, at 800 °C, formation of silicates is observed. Additionally, the electronic activation changes notably, transforming the baseline of the silicon wafer. Thus, we decided
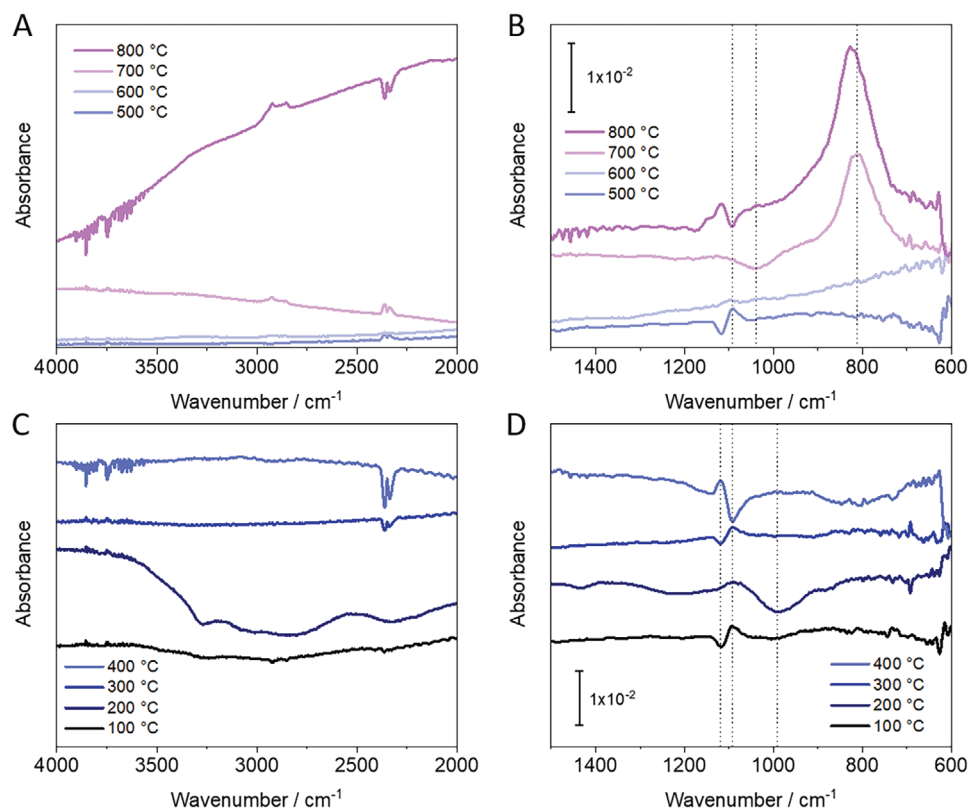
Figure 3. IR spectra as a function of the temperature. Measurements were always taken at room temperature. The sample (HAp/Si) was stepwise heated to the temperatures displayed in the image, with the spectra always referring to the previous temperature.

2400061 (4 of 10)

**ADVANCED
SCIENCE NEWS**

www.advancedsciencenews.com

**ADVANCED
MATERIALS
INTERFACES**

www.advmatinterfaces.de

Figure 4. Broadband IR response following annealing stepwise to 800 °C. At temperatures higher than 700 °C, the baseline seems to be overlaid with the absorbance of a two-component dielectric function.

to further take broadband IR measurements, to dig deeper into such transformation.[25–27]

To avoid the oxidation problem of ex situ electrical measurements, the electrical nature of the P atoms diffused into the bulk oxide can also be determined from in situ broadband IR measurements, which provide a complementary measure of the doping effect on the near-surface region. Therefore, we conducted temperature-dependent broadband IR measurements on a P-doped silicon wafer (**Figure 4**). The most noticeable aspect of our observations lies in the pronounced alterations to the baseline, notably manifest above 700 °C, and experiencing a drastic shift at 800 °C. These feature modifications strongly suggest the influence of phosphorus doping. In particular, the emergence of well-defined structures in the broadband IR spectra, especially beyond 800 °C, indicates a notable transformation in the dielectric properties of the material. To interpret these modifications of the spectra, we fitted the baseline using a two-component dielectric function. The Drude model, representing free carrier response, and the Lorentz model, capturing interband transitions, were employed as the main components. The fitting successfully shows that the dielectric properties can indeed be modeled with a two-component approach, although it is imperative to approach these fits critically, considering the potential complexities introduced by the Drude and Lorentz models. The observed changes are indicative of a doping threshold, highlighting the sensitivity of the dielectric response of the material to phosphorus doping levels. This insight may pave the way for a more nuanced understanding of the doping-induced modifications in the electronic structure of the silicon wafer and, consequently, its optical properties.

After the IR measurements, we can effectively state that the SiO_2 is still intact after all heating cycles. From this data, we can clearly conclude that the phosphorus was: i) transported through the silicon oxide barrier, ii) then diffused inside the oxide-free silicon, and iii) finally changed the electrical activity of the wafer.

Electrochemical impedance spectroscopy measurements as a function of temperature were also performed. Measurements were consistently conducted at RT on a P-doped silicon wafer. As shown in **Figure 5**, two semicircles are initially observed in the impedance plots, indicating a specific electrical behavior. However, after heating the sample to 700 °C, a notable transformation occurred, revealing three semicircles instead, and, remarkably, the sizes of these features were reduced by a factor of a thousand. Concurrently, phase measurements as a function of angular frequency demonstrated a significant shift to lower values, particularly in the range of 10^4 to 10^6 Hz beyond 700 °C. These observations suggest intricate changes in the electrical properties of the material, possibly linked to the phosphorus doping process or structural modifications induced at elevated temperatures. Further investigations and critical analysis are warranted to precisely elucidate the origin and implications of the observed phenomena, providing valuable insights into the dynamics of P-doped silicon under varying temperature conditions.

Finally, XPS measurements were performed on the samples. **Figure 6A** demonstrates the formation of silicates (as discussed by the IR data), through the XPS peak observed at 103.7 eV. Additionally, no oxide-free silicon can be observed, as opposed to the reference sample, which proves the existence of a thick sample layer over the wafer. To get a better picture of the doping process, we sputtered both samples until the Si 2p level of oxide-free silicon was displayed. A clear shift of ≈0.9 eV toward higher binding energies is observed for P-doped Si. In addition, the Si 2p level in the P-doped sample shows a broader, heavily asymmetric profile with a pronounced tail on the high binding energy side, which can originate from one or both of the following effects: i) a concentration gradient of the dopant throughout the XPS escape depth, or ii) coupling of the photoelectron to a continuum of electron–hole pair excitations, and iii) due to a Fano-like profile that is routinely observed in the photoemission spectra of conducting materials. Thus, the XPS data provide unambiguous evidence of diffusion of P through the native oxide layer into the Si bulk, leading to a significant level of *n*-type doping.

In order to investigate the dopant depth distribution, we performed depth profiling measurements using ToF-SIMS. **Figure 7** shows the obtained results for phosphorus dopant atoms in silicon wafers. The maximum concentration of phosphorus dopant atoms in silicon was measured to be 3×10^{21} cm^{-3}.
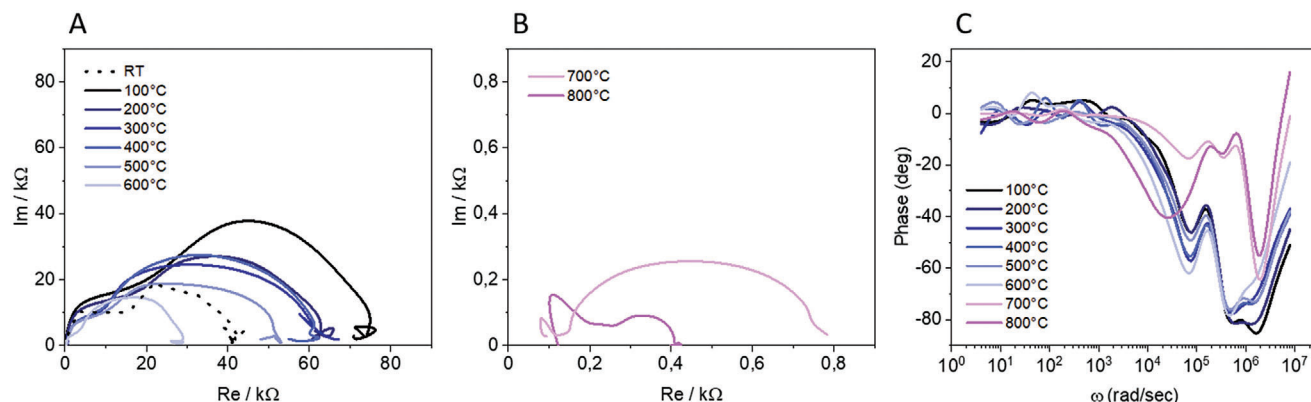
Finally, we aim to determine the activation efficiency of the phosphorus atoms using the Fermi level model. The activation efficiency (η) can be calculated using the formula:

$$\eta = \frac{n}{N_D} \times 100\% \tag{4}$$

where n is the concentration of activated phosphorus atoms and N_D is the total concentration of phosphorus dopant atoms. Subsequent calculations using this model yield an activation efficiency of ≈81%.

4.2. DFT Simulations of P-Doped Si

As mentioned in the Methods Section, we obtained the work function of P-doped Si(111) for different phosphorus concentrations and configurations, in order to correlate the computational

**ADVANCED
SCIENCE NEWS**

www.advancedsciencenews.com

**ADVANCED
MATERIALS
INTERFACES**
Open Access

www.advmatinterfaces.de

Figure 5. Panels A and B show Nyquist plots of the HAp/Si sample, measured after heating the system to the corresponding temperature. Panel C shows the corresponding phase as a function of the frequency.
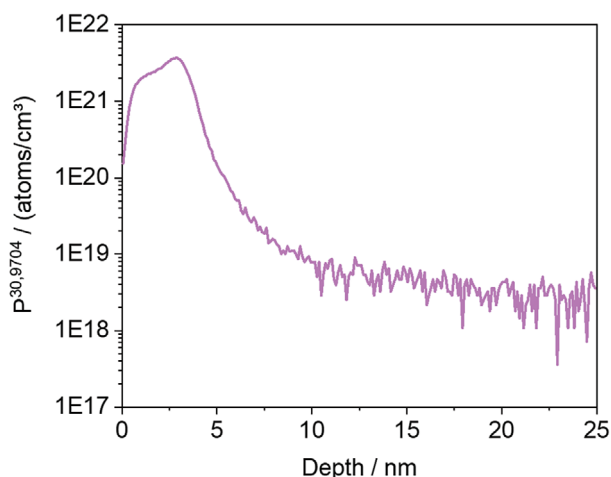
simulations with the differences in electrical activity after doping. A detailed analysis of the work functions of doped Si(111) will shed light on the effectiveness of shallow doping, especially to answer the question of whether there is an effective limit for doping.

The first question that needs to be addressed is the structure of doped Si(111), i.e., how a relatively dense and compact surface incorporates dopant atoms, whether on surface or sub-surface configurations. In this work, we limit the simulations to doping concentrations of 3×10^{20} atoms per cm^3, since that suffices to explore possible collaborative effects, as will be shown below. **Table 1** shows the obtained adsorption energies for the most relevant P—Si(111) configurations, as well as the corresponding work functions, whereas **Figure 8** depicts the geometrical structures.
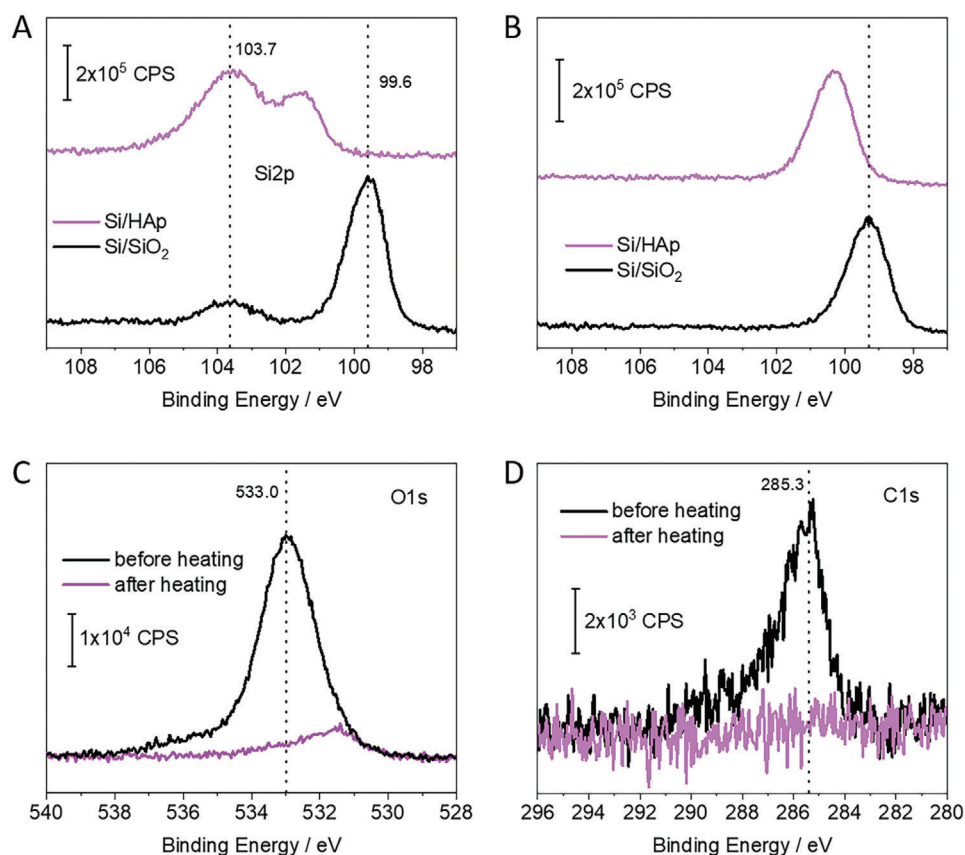
Figure 6. Panel A): Si 2p spectra of Si wafer prepared with HAp (after heating, magenta line) and Si wafer with native oxide as reference (black line). Panel B): XPS obtained after the samples were cleaned by sputtering with 3 keV Ar+, to remove the oxide at the surface. Panel C): O 1s spectra of Si wafer prepared with HAp before and after heating. Panel D): C 1s spectra of Si wafer prepared with HAp before and after heating.

**ADVANCED
SCIENCE NEWS**

www.advancedsciencenews.com

**ADVANCED
MATERIALS
INTERFACES**
Open Access

www.advmatinterfaces.de

Figure 7. ToF-SIMS of the HAp/Si interface after heating the sample to 900 °C. ToF-SIMS profiles of P in doped Si(111) were obtained using the P concentration. Clear incorporation of phosphorus into the Si after heating the HAp-terminated sample can be observed. In this case, most of the P is detected with SIMS.

Phosphorus can adsorb on Si(111) in various lattice sites, both over the surface and underneath. P atoms preferentially form tridentate configurations, bonding with 3 surface Si atoms. The P—Si bonding distance is 2.47 Å. Adsorption energies are −0.65 or −0.80 eV P^{-1} atom, depending on whether adsorption occurs in hollow sites or over a subsurface Si atom (see Figure 8). For this last configuration, the most thermodynamically favorable, the distance between the adsorbed P and the underneath Si atom is 2.87 Å, therefore forming a slightly distorted PSi$_4$ tetrahedra. Initial bidentate configurations spontaneously evolve into tridentate structures upon relaxation. Monodentate structures can also be formed (adsorption configuration in Table 1), although they show larger, less exothermic adsorption energies, 0.96 eV. That does not imply Si—P bond spontaneous dissociation, but that full surface coverage, monodentate phosphorus will segregate into bulk-like red phosphorus, the reference state. Using gas phase state references will likely render monodentate adsorption energies exothermic but, given the large variety of P-containing molecular precursors used in practice, gas phase references are

not practical except for specific settings. Finally, P can also be adsorbed in subsurface sites, bonding with 3 surface Si atoms and 1 atom from the second surface layer, forming a regular tetrahedral configuration with a Si—P bond distance of 2.30 Å. However, such a configuration is slightly less favorable due to the strain induced by the P atom diffusing underneath the surface. Substitutional configurations were not considered in this work due to the large kinetic energy barrier required to overcome in order to replace a Si lattice atom with the dopant P and, furthermore, differences in the work function with respect to interstitial P are negligible, as both cases represent subsurface P adsorption.

The adsorption process changes little for 2 P atoms because P atoms do not tend to cluster, especially inside the Si matrix, at least below a certain concentration threshold.[11] Indeed, as shown in Table 1 and Figure 8, the most favorable adsorption configuration includes 2 tridentate P atoms, but the distance between them is 4.71 Å, therefore transforming them into non-interacting adsorbates. The dimer configuration involves a weak interaction between the 2 P atoms, which are now 3.05 Å apart, but the adsorption energy is lower because one of the P atoms needs to adsorb in a bidentate mode. If one of the P atoms adsorbs forming a monodentate structure, the adsorption energy is slightly endothermic. Interestingly, subsurface adsorption of both P atoms does not lead to a thermodynamically exothermic process. Figure 8 shows graphically the strain induced on the Si(111) surface by the proximity of the 2 P atoms, which are both forming PSi$_4$ tetrahedral configurations in adjacent layers. This finding shows that, while P doping of Si is an exothermic process, it needs to be performed at low P concentrations for it to lead to thermodynamically viable phases. Adsorption of P saturates quickly. Indeed, the adsorption of 3 P atoms in a tridentate configuration shows an energy of −0.43 eV, which will remain constant until full surface coverage is achieved.

As mentioned above, we describe changes in the electrical activity by means of the work function, which represents a measure of the easiness of freeing electrons from the system, which is obviously an undesirable effect. The obtained work function for the pristine Si(111) surface is 4.58 eV. A priori, a correlation between adsorption energy and work function would be expected. Indeed, to consider that the stronger the binding the lower the Fermi level with respect to the vacuum level is a reasonable approach. However, the bandgap and, more specifically, the change in the gap with respect to the bare Si(111) surface due to the new states created by the dopants must also be considered. Table 1 shows both the obtained electronic bandgaps and the corresponding work function. Overall, the new orbitals created by the dopants are more localized than those of the host, which are delocalized over the Si atoms. Therefore, dopants inside the semiconductor matrix reduce the bandgap slightly more than those adsorbed on the surface (see Table 1). All the obtained bandgaps are likely underestimated at the GGA level of theory, but that does not affect the main conclusions of this study. P-doping transforms the Si into a direct-type semiconductor at the L point,[11] but P atoms tend to occupy Si lattice sites, thus increasing surface strain if adsorbed in subsurface configurations. However, a low concentration of shallow doping improves the electrical activity of the semiconductor noticeably. As can be seen in Table 1, even the low amount of doping considered increases the work function by almost 6% with respect to the bare Si(111) surface. Subsurface or
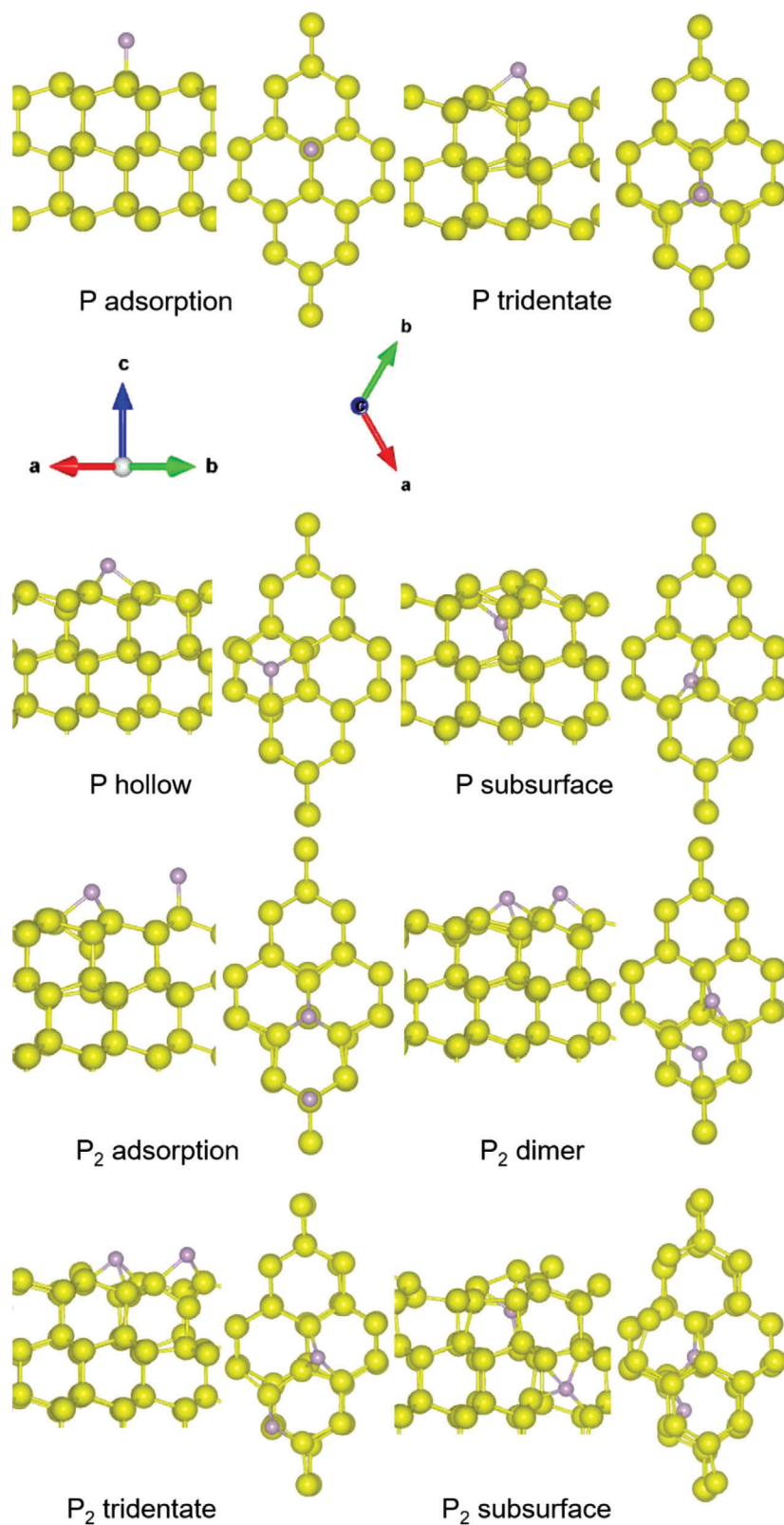
Table 1. Adsorption configurations for 1 and 2 phosphorus atoms on the Si(111) surface, adsorption energy per atom, electronic bandgap (spin up and down components), and work function. The work function of Si(111) is 4.58 eV.

# P atoms	Configuration	E_{ads} [eV]	Gap [eV]	φ [eV]
1	adsorption	0.96	0.58/0.36	4.61
1	tridentate	−0.80	0.58/0.61	4.75
1	hollow	−0.65	0.48/0.20	4.81
1	subsurface	−0.30	0.23/0.22	4.72
2	adsorption	0.06	0.61/0.64	4.84
2	dimer	−0.11	0.40/0.26	4.69
2	tridentate	−0.54	0.32/0.26	4.68
2	subsurface	1.25	0.34/0.26	4.55

ADVANCED
SCIENCE NEWS

www.advancedsciencenews.com

ADVANCED
MATERIALS
INTERFACES

www.advmatinterfaces.de

Figure 8. Top and side views of the most relevant adsorption configurations for 1 (upper panel) and 2 (lower panel) P atoms on the Si(111) surface. The legend of each configuration corresponds to the data shown in Table 1. Color code: pink (phosphorus) and yellow (silicon).

ADVANCED
SCIENCE NEWS

www.advancedsciencenews.com

ADVANCED
MATERIALS
**INTERFACES**
Open Access

www.advmatinterfaces.de

weakly bonding configurations are less effective than tridentate structures, as expected. However, increasing the doping density does not necessarily lead to a substantial improvement. The reason can be found in the amount of gap states introduced by different dopants. Given that clusterization lowers the binding energy, gap states created by isolated dopants can raise the Fermi level with respect to that of a single dopant, and even lead to an inversion of symmetry of the valence band maximum.[11] The largest value obtained for the work function corresponds to a mixed, two P atoms structure (adsorption configuration, see **Table 1**), with a strongly bound P atom in a tridentate configuration and a weakly bound, monodentate P atom.

To summarize, one can say that a, controlled, low amount of P doping can effectively introduce additional charge carriers (electrons), therefore increasing the carrier density and improving the electrical activity. However, there exists an upper limit to the effectiveness of this process, as demonstrated by our simulations. Therefore, mineral-containing doping agents can then be used to achieve ultra-shallow doping profiles, provided that the samples are conveniently annealed to overcome the kinetic barriers of the dissociation of the mineral oxide and subsequent diffusion of the dopants into the host semiconductor. Atomic control of the dopant adsorption sites provides an additional degree for optimization of the electrical activity.

The driving force for P diffusion into Si through the SiO_2 layer is the formation of P-Si_4 tetrahedra, which shows higher formation energy than that of the surface PO_4 species. A similar result was obtained in our previous work on O impurities at the InP-HfO_2 interface.[28] However, the energy required to break the P—O_4 bonds is relatively large, thus a high-temperature regime – 700 °C – is necessary to trigger the P diffusion process into the bulk Si. Once started, the transport of phosphorus atoms across the SiO_2 layer is relatively fast, with a kinetic barrier of only 1.5 eV for P diffusion into the Si bulk, according to our own calculations.[11] Then, P doping is successfully obtained by adsorption at different lattice sites, both over and underneath the surface, until saturation is achieved. Such saturation necessarily involves low P concentration, in order to obtain viable P-Si phases, as demonstrated above.

Calcium and oxygen have very limited solubility in silicon at high temperatures, which thermodynamically favors their remaining in the surface layer rather than diffusing into the silicon substrate. The formation of wollastonite ($CaSiO_3$) at the surface suggests that calcium reacts with silicon dioxide (SiO_2) or other silicon compounds available at the surface, consuming Ca and O locally and preventing their diffusion into the bulk silicon. At 900 °C, the diffusion rates of calcium and oxygen in silicon are relatively low compared to phosphorus, which has a higher diffusivity in silicon. This discrepancy in diffusion rates can contribute to the surface localization of calcium and oxygen. The larger ionic radii of Ca^{2+} and O^{2-} compared to the smaller P atoms might hinder their mobility and diffusion into the silicon lattice.

In our study, a thin layer of hydroxyapatite was deposited onto a silicon (Si) wafer and subsequently subjected to rapid temperature annealing (RTA) at 900 °C. During this thermal process, phosphorus (P) from the hydroxyapatite diffuses into the silicon substrate, while calcium (Ca) and oxygen (O) remain largely immobile and do not penetrate the wafer. This selective diffusion is primarily driven by thermodynamic factors. As a result of the dif-
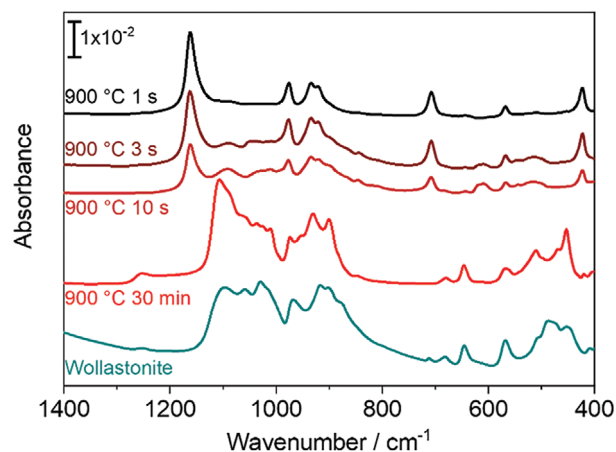
Figure 9. From the top to the bottom: Absolute IR spectra of heating periods of Hydroxyapatite compared to the spectrum of Wollastonite (both prepared by T-BAG).

fusion of phosphorus and the concurrent lack of significant calcium and oxygen movement, wollastonite ($CaSiO_3$) forms on the surface of the wafer. The presence of wollastonite is confirmed by infrared (IR) spectroscopy (see **Figure 9**), which provides conclusive evidence of its formation, thereby supporting the thermodynamically driven transformation.

A diverse set of minerals can be used to effectively form metal silicates in contact with silicon oxide. This process is mainly thermodynamically driven and has already been well investigated using the example of calcium silicate. One of the thermodynamically most stable calcium silicate phases is wollastonite ($CaSiO_3$).[12,29] The main advantage of such formed phases as a reaction product is that they do not have to be etched with HF in the last step of semiconductor process etching, direct use of mineral acids such as HCl or H_2SO_4 suffices to remove undesired reaction byproducts.[30] The doping methodology employed, utilizing the T-BAG technique for sample fabrication, is not without its inherent limitations. While this method is widely utilized for its simplicity and efficacy, it is crucial to acknowledge its drawbacks, particularly the tendency toward an uneven distribution of dopants over the semiconductor material. This phenomenon results in an inherent inhomogeneity across the sample, thereby imposing clear constraints on the accuracy and reliability of the doping process. Consequently, while the T-BAG method offers expediency in sample preparation, its propensity for non-uniform doping distribution underscores the necessity for careful consideration and potential refinement in future doping strategies.[31–33]

5. Conclusion

In this work, we have shown the doping of silicon performed without using any toxic chemical substances, such as HF or $POCl_3$. The process was carried out in the following way: First, the wafers were cleaned. In the second step, the doping material was applied using the T-BAG method. Finally, both were heated together. In the low-temperature regime (100–500 °C), all organic components from the mineral were released. The transport of the phosphate through the native silicon oxide is driven by a phase

transformation into a more stable thermal oxide. At 700 °C, diffusion of P into the sub-surface region of oxide-free silicon is observed to begin. From our IR combined with EIS and XPS measurements, it can be concluded that the phosphorus was 1) transported through the silicon oxide barrier, 2) then diffused inside the oxide-free silicon and 3) finally changed the electrical activity. Our DFT simulations have demonstrated the atomistic mechanism behind the optimization of the electrical activity via P doping. Precise control of the dopant concentration as well as the adsorption configurations offer two specific and clear pathways for control and improvement of the resulting semiconductor matrix structure performance.

Acknowledgements

Conflict of Interest

The authors declare no conflict of interest.

Data Availability Statement

The data that support the findings of this study are available from the corresponding author upon reasonable request.

Keywords

[1] O. Hazut, A. Agarwala, I. Amit, T. Subramani, S. Zaidiner, Y. Rosenwaks, R. Yerushalmi, *ACS Nano* **2012**, *6*, 10311.
[2] O. Hazut, B. C. Huang, A. Pantzer, I. Amit, Y. Rosenwaks, A. Kohn, C. S. Chang, Y. P. Chiu, R. Yerushalmi, *ACS Nano* **2014**, *8*, 8357.
[3] J. C. Ho, R. Yerushalmi, Z. A. Jacobson, Z. Fan, R. L. Alley, A. Javey, *Nat. Mater.* **2008**, *7*, 62.
[4] J. C. Ho, R. Yerushalmi, G. Smith, P. Majhi, J. Bennett, J. Halim, V. N. Faifer, A. Javey, *Nano Lett.* **2009**, *9*, 725.
[5] R. C. Longo, K. Cho, W. G. Schmidt, Y. J. Chabal, P. Thissen, *Adv. Funct. Mater.* **2013**, *23*, 3471.
[6] R. A. Beckman, E. Johnston-Halperin, N. A. Melosh, Y. Luo, J. E. Green, J. R. Heath, *J. Appl. Phys.* **2004**, *96*, 5921.
[7] M. A. Hughes, Y. Fedorenko, B. Gholipour, J. Yao, T. H. Lee, R. M. Gwilliam, K. P. Homewood, S. Hinder, D. W. Hewak, S. R. Elliott, R. J. Curry, *Nat. Commun.* **2014**, *5*, 5346.
[8] E. C. Jones, E. Ishida, *Materials Science and Engineering: R: Reports* **1998**, *24*, 1.
[9] J. W. Lee, Y. Sasaki, M. J. Cho, M. Togo, G. Boccardi, R. Ritzenthaler, G. Eneman, T. Chiarella, S. Brus, N. Horiguchi, G. Groeseneken, A. Thean, *Appl. Phys. Lett.* **2013**, *102*, 223508.
[10] B. Mehta, M. Tao, *J. Electrochem. Soc.* **2005**, *152*, G309.
[11] P. Thissen, K. Cho, R. C. Longo, *ACS Appl. Mater. Interfaces* **2017**, *9*, 1922.
[12] N. Giraudo, P. Krolla-Sidenstein, S. Bergdolt, M. Heinle, H. Gliemann, F. Messerschmidt, P. Brüner, P. Thissen, *J. Phys. Chem. C* **2015**, *119*, 10493.
[13] J. Schmitz, M. van Gestel, P. Stolk, Y. Ponomarev, F. Roozeboom, J. Van Berkum, P. Zalm, P. Woerlee, In *Ultra-shallow junction formation by outdiffusion from implanted oxide*, San Francisco, CA, USA, December, **1998**.
[14] P. A. Stolk, J. Schmitz, F. N. Cubaynes, A. C. M. C. v. Brandenburg, J. G. M. v. Berkum, W. G. v. d. Wijgert, F. Roozeboom, In *The Effect of Thin Oxide Layers on Shallow Junction Formation*, September, **1999**.
[15] A. Vega, P. Thissen, Y. J. Chabal, *Langmuir* **2012**, *28*, 8046.
[16] F. Schnetzer, P. Thissen, N. Giraudo, K. Emmerich, *J. Phys. Chem. C* **2016**, *120*, 15282.
[17] F. Schnetzer, C. T. Johnston, G. S. Premachandra, N. Giraudo, R. Schuhmann, P. Thissen, K. Emmerich, *ACS Earth Space Chem.* **2017**, *1*, 608.
[18] G. Kresse, J. Hafner, *Phys. Rev. B* **1993**, *47*, 558.
[19] G. Kresse, J. Furthmüller, *Phys. Rev. B* **1996**, *54*, 11169.
[20] G. Kresse, D. Joubert, *Phys. Rev. B* **1999**, *59*, 1758.
[21] J. P. Perdew, K. Burke, M. Ernzerhof, *Phys. Rev. Lett.* **1996**, *77*, 3865.
[22] H. J. Monkhorst, J. D. Pack, *Phys. Rev. B* **1976**, *13*, 5188.
[23] S. Kc, R. C. Longo, K. Xiong, K. Cho, *J. Electrochem. Soc.* **2014**, *161*, F3104.
[24] A. Simon, H. Borrmann, J. Horakh, *Chem. Ber.* **1997**, *130*, 1235.
[25] V. M. Kashkarov, D. L. Goloshchapov, A. N. Rumyantseva, P. V. Seredin, E. P. Domashevskaya, I. A. Spivakova, B. R. Shumilovich, *J.Surf. Invest. X-ray, Sync. Neutr. Tech.* **2011**, *5*, 1162.
[26] R. C. Longo, E. C. Mattson, A. Vega, W. Cabrera, K. Cho, Y. J. Chabal, P. Thissen, *Chem. Mater.* **2016**, *28*, 1975.
[27] R. Tian, O. Seitz, M. Li, W. Hu, Y. J. Chabal, J. Gao, *Langmuir* **2010**, *26*, 4563.
[28] S. Kc, H. Dong, R. C. Longo, W. Wang, K. Xiong, R. M. Wallace, K. Cho, *J. Appl. Phys.* **2014**, *115*, 023703.
[29] S. Sanna, W. G. Schmidt, P. Thissen, *J. Phys. Chem. C* **2014**, *118*, 8007.
[30] R. C. Longo, K. Cho, P. Brüner, A. Welle, A. Gerdes, P. Thissen, *ACS Appl. Mater. Interfaces* **2015**, *7*, 4706.
[31] B. C. Popere, B. Russ, A. T. Heitsch, P. Trefonas, R. A. Segalman, *Adv. Mater. Interfaces* **2015**, *2*, 1500421.
[32] M. L. Hoarfrost, K. Takei, V. Ho, A. Heitsch, P. Trefonas, A. Javey, R. A. Segalman, *J. Phys. Chem. Lett.* **2013**, *4*, 3741.
[33] M. Perego, G. Seguini, E. Arduca, A. Nomellini, K. Sparnacci, D. Antonioli, V. Gianotti, M. Laus, *ACS Nano* **2018**, *12*, 178.